ACS OMEGA

Article

Cite This: ACS Omega 2018, 3, 17895−17903

http://pubs.acs.org/journal/acsodf

[((*R*)-$C_8H_{12}N)_4$][Bi_2Br_{10}] and [((*S*)-$C_8H_{12}N)_4$][Bi_2Br_{10}]: Chiral Hybrid Bismuth Bromides Templated by Chiral Organic Cations

Tae Hwan Moon, Seung-Jin Oh, and Kang Min Ok*

Department of Chemistry, Chung-Ang University, 84 Heukseok-ro, Dongjak-gu, Seoul 06974, Republic of Korea

Supporting Information

ABSTRACT: Single crystals of organically templated chiral bromobismuthates(III), [((*R*/*S*)-$C_8H_{12}N)_4$][Bi_2Br_{10}], have been grown for the first time via a slow evaporation method. Each of the chiral molecular compound consists of (*R*) or (*S*)-1-phenylethylammonium ([$C_8H_{12}N]^+$) cations and [$Bi_2Br_{10}]^{4-}$ anions. Both the title compounds reveal thermal and moisture stabilities up to ca. 220 °C and over 1 month, respectively. The newly prepared Bi^{3+}-based organic−inorganic hybrid materials show optical band gap of ca. 2.88 eV. The noncentrosymmetric [((*R*)-$C_8H_{12}N)_4$][Bi_2Br_{10}] and [((*S*)-$C_8H_{12}N)_4$][Bi_2Br_{10}] exhibit second harmonic generation efficiency of ca. 20 times that of α-SiO_2 and are type I nonphase matchable. Uniformly deposited thin films of [((*R*)-$C_8H_{12}N)_4$]-[Bi_2Br_{10}] and [((*S*)-$C_8H_{12}N)_4$][Bi_2Br_{10}] have been also successfully obtained by a simple spin-coating method. The circular dichroism spectra for both reported thin films are symmetrical, attributable to the corresponding Cotton effect. The selectively deposited chiral thin films are expected to be used as a useful platform for various surface reactions and interface engineering.

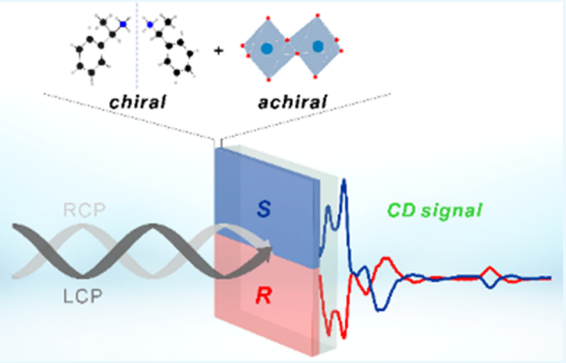

INTRODUCTION

Recently, organic−inorganic hybrid materials (OIHMs) have gained immense interest owing to the remarkable optoelectronic properties[1,2] and their numerous applications in light-emitting diodes,[3−5] photodetectors,[6−8] photocatalysts,[9−11] transistors,[12] nanowire lasers,[13−15] and photovoltaic devices.[16−19] The technologically important applications mainly originate from the materials' excellent physical properties such as intense light absorption, weakly bound charge-transfer excitons, and long charge diffusion lengths.[20−22] For example, methylammonium lead halides-based hybrid perovskite solar cells with a high power conversion efficiency of 22.1% have drawn remarkable attention as next-generation photovoltaics.[23] Chiral lead halides synthesized with chiral amines with perovskite-like materials have also exhibited interesting optoelectronic applications including photoluminescence and ferroelectricity.[24,25] Unfortunately, however, lead in the hybrid perovskites is highly toxic and has an adverse environmental impact. Therefore, hybrid perovskites containing less toxic and relatively harmless metal cations have been sought extensively. Among many, Bi^{3+}-based OIHMs have been considered as good replacements of conventional Pb^{2+}-based absorbers due to their lower toxicity.[26] In addition, similar interesting materials' properties arising from the trivalent Bi^{3+} cations containing the same $6s^2$ lone pair electrons as those in the divalent Pb^{2+} cations are expected from Bi^{3+}-based OIHMs. A highly air-stable methylammonium bismuth iodide, [$(CH_3NH_3)_3$][Bi_2I_9], has been recently reported as a promising constituent of lead-free solar cell absorbers.[27] Hybrid compounds consisting of halobismuthates(III) and various organic molecules are in fact of great interest due to their additional optical and electronic properties such as nonlinear optical (NLO) behavior,[28−33] photoluminescence,[30,34] and ferroelectricity.[35,36] In particular, second harmonic generation (SHG), which is one of the second-order NLO properties, enables the application of optical switches, frequency doubling, and optical data storage devices.[37] However, the interesting characteristics are only expected when the materials crystallize in macroscopic noncentrosymmetric (NCS) structures.[38] Although quite a lot of OIHMs have been discovered thus far, most of the crystalline materials exhibit centrosymmetric (CS) structures. To induce overall NCS structures of OIHMs more effectively, we have introduced chiral organic cations as structure-directing agents during the synthesis stage, where a facile formation of asymmetric anion backbones and the subsequent tunable optical and electronic properties could be anticipated. By doing so, we were able to successfully synthesize two novel 1-phenylethylammonium bromobismuthates(III), (*R*)/(*S*)-[$C_8H_{12}N]_4$[Bi_2Br_{10}]. We also successfully fabricated the chiral OIHMs as thin films on glass substrates by a simple spin-coating method and investigated their optical properties through solid-state CD spectroscopy. The uniformly deposited chiral thin films indeed suggest applicability of the materials to

Received: October 19, 2018
Accepted: December 7, 2018
Published: December 20, 2018

DOI: 10.1021/acsomega.8b02877
ACS Omega 2018, 3, 17895−17903

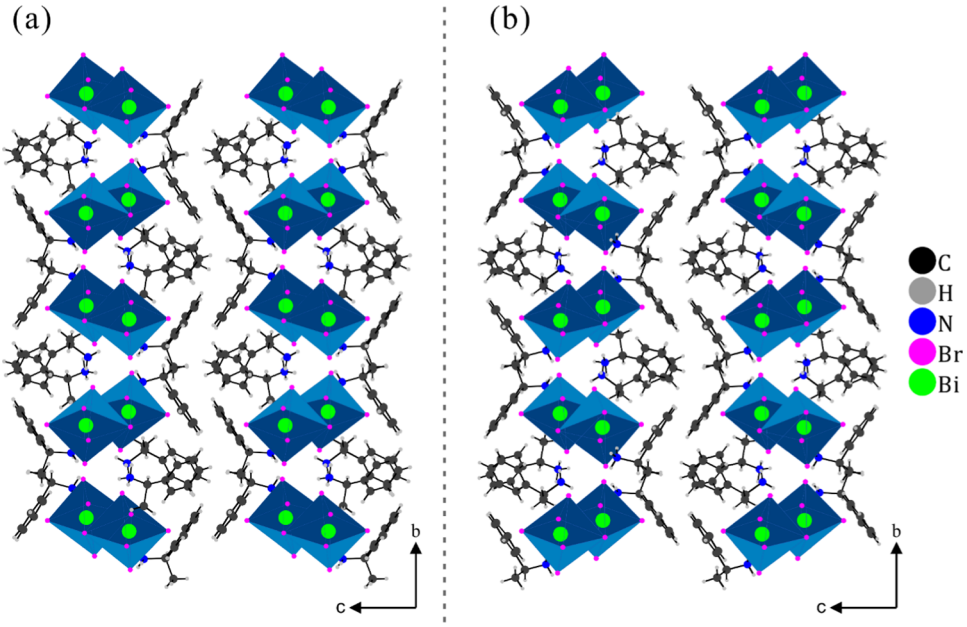

Figure 1. Ball-and-stick and polyhedral representations of (a) (*R*)-**1** and (b) (*S*)-**1** at room temperature, projected along the *a*-axis. Note that the two compounds (*R*)-**1** and (*S*)-**1** are enantiomorphic to each other.

the optoelectronic devices. Herein, we present the synthesis, crystal structures, elemental analysis, thermal and moisture stability, and a variety of bulk and thin film characteristics of novel chiral Bi-based OIHMs.

RESULT AND DISCUSSION

Structures. Yellow large plate crystals of (*R*)-**1** and (*S*)-**1** have been grown in high yields (86.2%) through a slow evaporation method. Single-crystal X-ray diffraction (SCXRD) suggests that both the title compounds, (*R*)-**1** and (*S*)-**1**, crystallize in the polar monoclinic space group, $P2_1$ (no. 4) with the same unit cell parameters. Interestingly, the chirality of the chiral organic cations has determined the chirality of the reported complexes. Because the structures of both (*R*)-**1** and (*S*)-**1** are basically the same except for the chirality, only the detailed structural description of (*R*)-**1** is provided here. (*R*)-**1** can be classified as a molecular compound that is composed of (*R*)-1-phenylethylammonium ($[C_8H_{12}N]^+$) cations and $[Bi_2Br_{10}]^{4-}$ anions (Figure 1). As seen in Figures 2 and S2, four unique (*R*)-1-phenylethylammonium cations exist in the unit cell, where all of the chiral centers, i.e., C(7), C(15), C(23), and C(31) are (*R*)-configurations and responsible for the overall chirality of (*R*)-**1**. Two unique Bi^{3+} cations in an asymmetric unit are coordinated by six bromide ligands in distorted $BiBr_6$ octahedral coordination environments. The observed Bi−Br bond distances and Br−Bi−Br bond angles are 2.6826(16)−3.1376(15) Å and 82.61(3)−179.29(5)°, respectively. Each $BiBr_6$ octahedron shares its edge through Br(5) and Br(6) and forms $[Bi_2Br_{10}]^{4-}$ anionic dimers. It should be noted that the edge-shared $[Bi_2Br_{10}]^{4-}$ dimers are strongly distorted. In other words, whereas the bond lengths between Bi^{3+} and terminal Br^- are shorter [2.6826(16)−2.8637(16) Å], those between Bi^{3+} and bridging Br^- are significantly longer [3.0213(12)−3.1376(15) Å] attributed to a trans effect.[39] Thus, the stereochemically rather less-active lone pairs on Bi^{3+} seem to be pointing to the edges of $[Bi_2Br_{10}]^{4-}$ dimers. In addition, the $BiBr_6$ octahedral distortion should be influenced by the hydrogen-bonding interactions between N−H in (*R*)-1-phenylethylammonium cations and Br^- (N−H···Br). Specifically, all the NH_3^+ cations in (*R*)-1-phenylethylammonium group interact with Br^- ligands in axial position or bridging Br^- ligands in $[Bi_2Br_{10}]^{4-}$ octahedra. Thus, the bond distances between Bi^{3+} and Br^- ligands in the axial position [2.8343(16)−2.8637(16) Å] are longer than those between Bi^{3+} and Br^- ligands in the equatorial position [2.6826(16)−2.7542(12) Å] and the polyhedra are tilted toward the NH_3^+ cations (Figure S3). Detailed hydrogen bonding interactions are tabulated in the Supporting Information. The bond valence sum calculations[40] result in values of 3.21−3.24, 0.60−0.62, and 0.52−0.84 for Bi^{3+}, bridging Br^-, and terminal Br^-, respectively (Table S2). The lower bond valence values for the bridging Br^- ligands, Br(5) and Br(6), should be due to the hydrogen-bonding interactions.

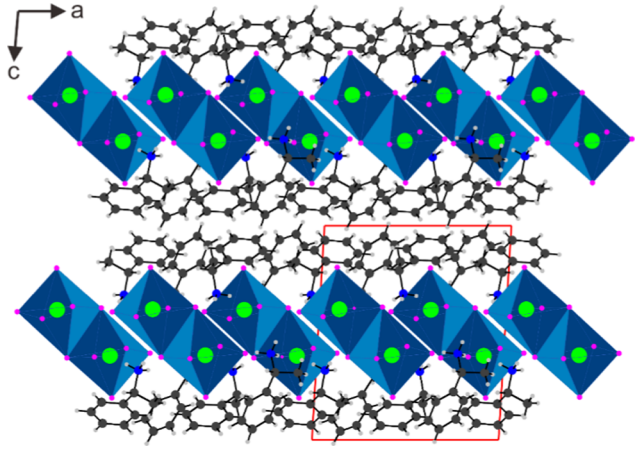

Figure 2. Packing diagram of (*R*)-**1** at room temperature, projected along the *b*-axis.

Thermal and Humidity Stability. Thermal analyses performed on the ground samples of compound (*R*)-**1** revealed that the material is thermally stable up to ca. 220 °C (Figure S4). Upon further heating, the compound continuously lost

DOI: 10.1021/acsomega.8b02877
ACS Omega 2018, 3, 17895−17903

weight and completely decomposed and evaporated by ca. 600 °C. Moisture stability for thin film and polycrystalline samples of compound (*R*)-**1** was also tested. Both thin film and polycrystalline samples of (*R*)-**1** were exposed at conditions with 95 ± 5 and 65% relative humidity, respectively, for over 30 days. Powder X-ray diffraction (PXRD) patterns for both polycrystalline and thin film samples of (*R*)-**1** exposed to humidity for 30 days are exactly same as that of the dried authentic sample, which indicates that both polycrystalline and thin film samples of (*R*)-**1** are very robust to moisture (Figures 3 and S5).

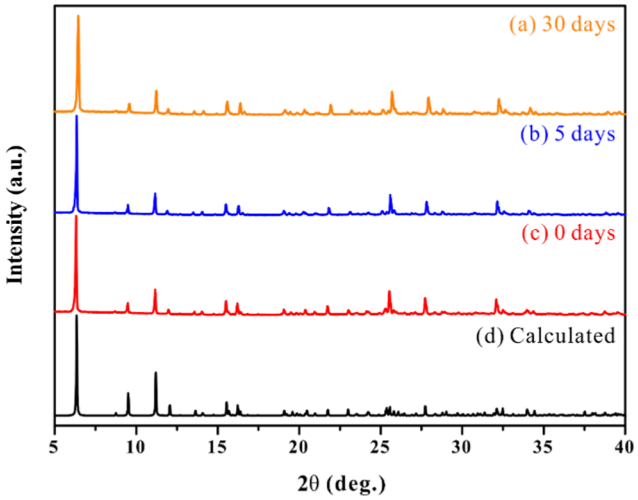

Figure 3. (a–c) PXRD patterns of compound (*R*)-**1** exposed to humidity (95 ± 5% relative humidity) and (d) calculated patterns. All the measured PXRD patterns for the samples exposed to humidity for long time are consistent with the calculated pattern, indicating the compound is robust to moisture.

IR and UV–Vis Diffuse Reflectance Spectroscopy. The constituting functional groups in the organic cations were successfully identified by the IR spectroscopy. The existence of ammonium overtones near 2500 and 2000 cm^{-1}, and the presence of stretching vibrations of Ar–H and C=C at around 3108 and 1450–1600 cm^{-1}, indicating the aromatic character were confirmed by the presence of 1-phenylethylammonium cations in the compounds (Figure S6).

The experimental optical band gap was determined by converting the UV–vis diffuse reflectance spectrum of the chiral compound to the absorbance spectrum by the Kubelka–Munk transformation and extrapolating the $F(R)$ versus energy (eV) curve to zero. The optical band gap and the cutoff wavelength are calculated to be ca. 2.88 eV and 427 nm, respectively (Figure 4). The gentle curves found in the UV–vis absorption spectra suggest that the band edge of the reported chiral compounds may have indirect band gaps.[41] The band gaps of the reported chiral compounds are similar to those of other various organic–inorganic halide materials.[30,42−44] Because the band gaps of a series of halides compounds are varied by changing the constituting halides (Cl^-, Br^- and I^-), the related materials can be used in optoelectronic devices by controlling the stoichiometry of halide anions.

Chirality in Thin Films. Compounds (*R*)-**1** and (*S*)-**1** are confirmed to be (*R*)- and (*S*)-configurations at the benzylic carbon site, i.e., the chiral center of 1-phenylethylammonium cation, by SCXRD analysis. We further investigated if the chiral

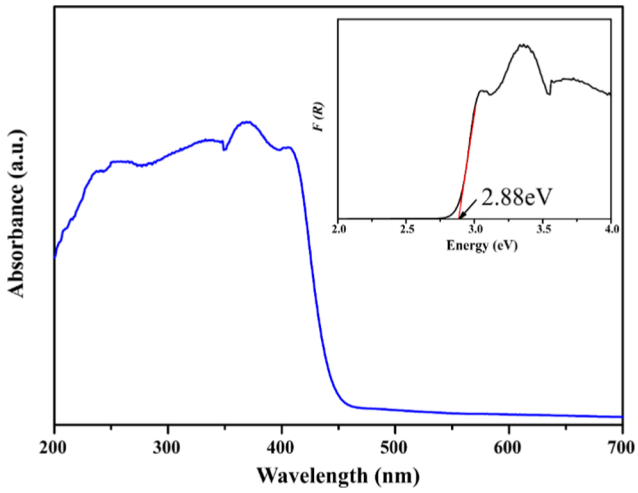

Figure 4. UV–vis diffuse reflectance spectrum and calculated optical band gap of compound (*R*)-**1**. Absorbance was observed from the cutoff wavelength of 429 nm (2.88 eV) to the deep-ultraviolet range (wavelength below 350 nm).

crystalline compounds could be uniformly deposited on substrates as thin films with the same chemical compositions. First, each synthesized chiral compound was redissolved in *N*,*N*′-dimethylformamide (DMF) to form precursor solutions, and the corresponding thin films with the thickness of several hundred nanometers were successfully deposited on glass substrates through spin-coating processes (Figure 5). The

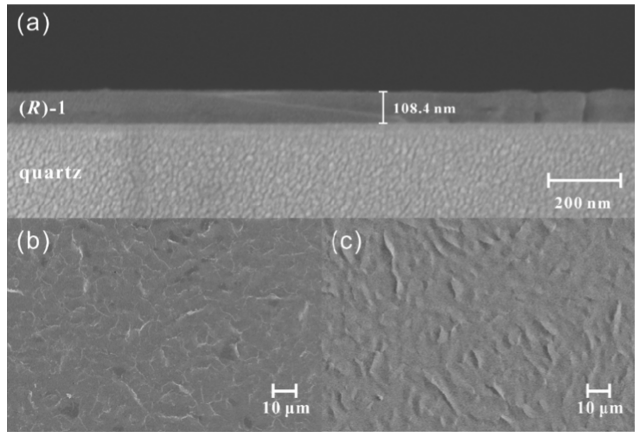

Figure 5. Field emission scanning electron microscopy (FE-SEM) image of (a) cross-sectional and (b, c) surface for (*R*)-**1** thin films with quartz substrates. The thickness of the spin-coated film was ca. 100 nm.

energy-dispersive X-ray (EDX) analyses on the chiral thin films revealed that the compositions of the prepared films were also the same as those of single crystals (Figure S1b). The PXRD analysis of thin films indicated that the crystals grow along the (h00) direction (Figure 6). In the case of thin films of homogeneously deposited chiral compounds, the preferred orientation strongly occurs along a specific direction. The optical activity of thin films was also analyzed by transmittance circular dichroism (CD) analysis. Both (*R*)-**1** and (*S*)-**1** were deposited on quartz substrates with high transmittance up to the wavelength range of the deep UV region because the absorbance of chiral compounds (*R*)-**1** and (*S*)-**1** were observed in the low-UV region (wavelength below 400 nm).

DOI: 10.1021/acsomega.8b02877
ACS Omega 2018, 3, 17895−17903

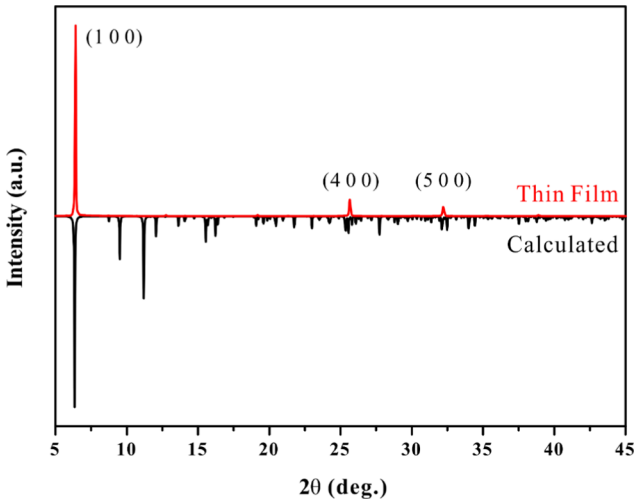

Figure 6. PXRD patterns of compound (***R***)-**1** thin film fabricated on a quartz substrate and calculated pattern from SCXRD data. Note the pattern for (***R***)-**1** thin film reveals a strong preferred orientation along the *a*-axis.

Left and right circularly polarized lights (CPL) with wavelengths from 400 to 180 nm were irradiated on the chiral thin films and the CD spectra were determined by the difference in the absorption of CPL (Figure 7). The CD spectra of (***R***)-**1** and (***S***)-**1**, which are symmetrical to each other (mirrored CD signal), clearly demonstrate that the two chiral thin films have different optical properties and contain absolute configuration of *R* and *S*, respectively. The CD signal of thin film (***R***)-**1** is first observed in the range of 380−317 nm attributed to CPL absorption, and the value of CD signal is inverted at 353 nm. Then, the CPL absorption increases to 240 nm and decreases slightly at around 200 nm; however, the absorption of CPL is maintained. The CD signal is significantly reversed near 231 and 212 nm. As described above, the phenomenon that the signal changes in the opposite direction, whereas the absolute magnitude of the optical rotation crosses zero at the maximum absorbance (353 nm) is called the Cotton effect.[45,46] Whereas the (***R***)-**1** thin film exhibits a positive Cotton effect after optical rotation decreases first as the wavelength decreases, the (***S***)-**1** thin film exhibits the opposite negative Cotton effect (green area in Figure 7). Also, multiple Cotton effect curves were observed because the absorption does not increase or decrease constantly in the range of 260−180 nm (yellow area in Figure 7). The maximum absorption wavelengths of free (*R*)-(+)-1-phenylethylamine ((*R*)-1-PEA) and (*S*)-(−)-1-phenylethylamine ((*S*)-1-PEA) organics were reported to be about 260 nm.[24,47,48] A complete change of CD signals for thin films of compounds (***R***)-**1** and (***S***)-**1** indicates that the CD signals are not just caused by the simple chiral organic cations but by more complex interactions. Anisotropy factors (*g*) were calculated from the wavelength range of 400−180 nm to obtain the concentration-independent values (Figure S7). The maximum anisotropy factor of (***R***)-**1** and (***S***)-**1** thin films was 8.02×10^{-4} and 1.28×10^{-3} at 203 nm, respectively, which are similar to the values observed from other chiral QDs or hybrid semiconductor materials.[49,50]

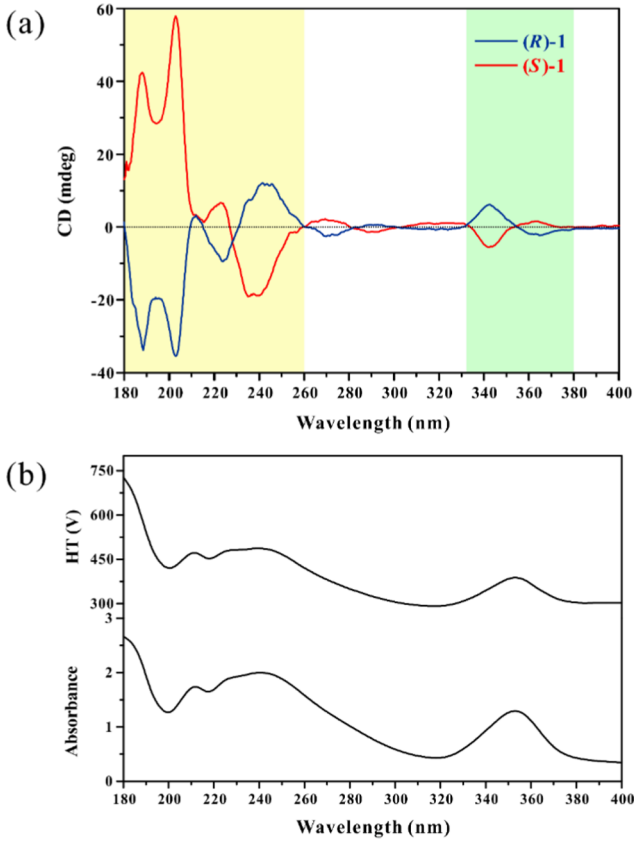

Figure 7. (a) Transmittance CD spectra of (***R***)-**1** and (***S***)-**1** thin films with quartz substrates. Thin films of compounds (***R***)-**1** and (***S***)-**1** reveal different absorption of circular polarized light, which results in symmetric spectra to each other. (b) High-tension (HT) voltage and absorbance spectrum of (***R***)-**1** film.

Electronic Band Gap Calculations. Density function theory (DFT) calculations were performed to investigate the electronic structure of compound (***R***)-**1**. Partial density of state (PDOS) was calculated using an optimized crystallographic geometry. The calculated Fermi level was fixed at 0 eV and the energy level of each atomic orbital was adjusted. The valence band maximum (VBM) and the conduction band minimum (CBM) energy were calculated to be −1.76 and 1.44 eV, respectively (Figure 8). The slight overestimation of the calculated band gap energy (3.2 eV) compared to the measured optical band gap (2.88 eV) is possibly attributed to the exclusion of the spin−orbit coupling effect in the self-consistent field (SCF) calculation.[29,51] As seen in the partial density of state (PDOS), the s- and p-orbitals of carbon and nitrogen are mostly overlapped with the 1s orbital of hydrogen, which well accounts for C−H and N−H covalent bonds (Figure 8). Orbitals of bismuth and bromine are also fully overlapped, indicating that the strong Bi−Br covalent bonds can form an octahedral structure. VBM originates mostly from Br 4p orbital, and CBM originates from Bi 6p orbital. Therefore, it can be seen that the inorganic anion, bromobismuthates(III), has a significant influence on the band gap energy. C 2p orbital has a considerable effect on both VBM and CBM, which were derived from the π-bonding orbital and π^*-antibonding orbital, respectively, in the benzene ring of aromatic organic molecules. Hence, once the band gap of the OIHM is carefully controlled by changing the constituting halides and organic molecules, various optoelectronic applications would be possible.

Powder Second Harmonic Generation (SHG) Measurements. The nonlinear optical (NLO) properties were measured because two chiral compounds with (*R*)- and (*S*)-

DOI: 10.1021/acsomega.8b02877
ACS Omega 2018, 3, 17895−17903

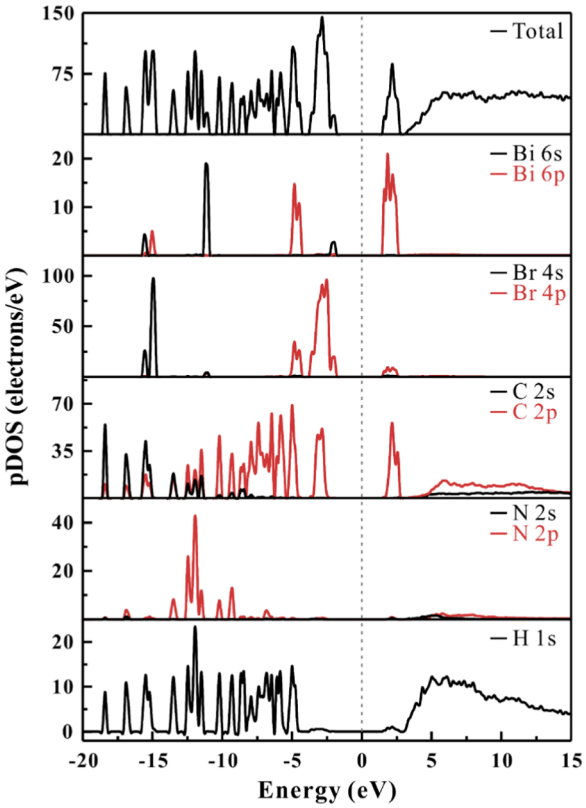

Figure 8. Partial density of states (PDOS) calculation of compound (*R*)-**1**. The solid line at 0 eV represents the Fermi level.

configuration crystallized in the polar space group, $P2_1$. The plot of the SHG intensity measured at each distinct particle size ranges for the ground crystals of (*R*)-**1** is shown in Figure 9. As seen in Figure 9, the SHG efficiency of (*R*)-**1** increased to near the coherence length of the compound, 63 μm, and then decreased rapidly, i.e., type I nonphase matchable.[52] (*R*)-**1** also exhibited an SHG efficiency of ca. 20 times that of polycrystalline α-SiO_2. In fact, the development of phase-matchable polar materials with large NLO coefficients by careful alignment of asymmetric units should be critical for

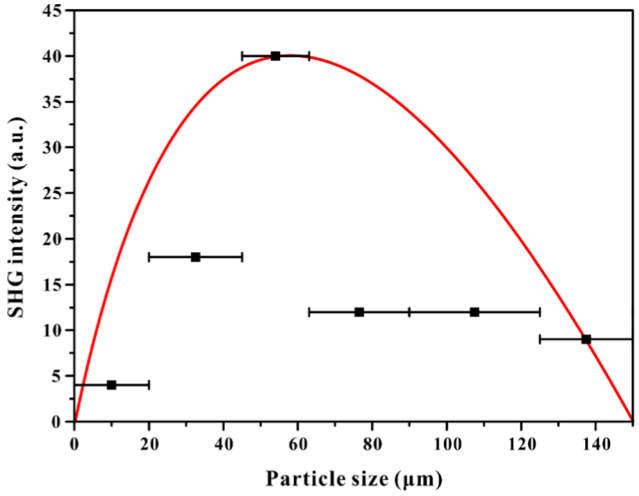

Figure 9. Particle size dependence of second-harmonic generation (SHG) intensity for compound (*R*)-**1**. The curve is drawn to guide eyes.

applications. The SHG effect of polar materials can be explained by the direction and magnitude of the dipole moment.[53−55] The dipole moment directions of bismuth octahedra are shown in Figure S8. Dipole moment calculations for (*R*)-**1** indicate that the approximate direction of $Bi(1)Br_6$ and $Bi(2)Br_6$ octahedra are (101) and $(\bar{3}\bar{1}3)$, respectively (Table S5). Also, the energy calculations of four 1-phenylethylammonium cations using the computer program Gaussian resulted in dipole moments along the four approximate directions of $(\bar{2}0\bar{1})$, (201), $(3\bar{1}\bar{1})$, and (201). Thus, an overall dipole moment of 16.5 D is observed along the approximate $(3\bar{1}\bar{1})$ direction.

CONCLUSIONS

In summary, two polar chiral bismuth bromides, $[((R)\text{-}C_8H_{12}N)_4][Bi_2Br_{10}]$ and $[((S)\text{-}C_8H_{12}N)_4][Bi_2Br_{10}]$, which are optical isomers, were synthesized through a mild solution chemistry method using chiral organic structure-directing cations. The new Bi-based organic−inorganic hybrid materials reveal the chiral NCS structures affected by chiral organic molecules. The second-order NLO properties resulting from this structural NCS were confirmed by measuring the powder SHG. The direction and magnitude of the dipole moments for $BiBr_6$ octahedra and 1-phenylethylammonium cations were calculated to determine the origin of SHG. The title compounds were robust to moisture for more than 1 month and thermally stable up to 220 °C. High-quality uniform thin films of the reported chiral materials were also successfully obtained on glass substrates by simple spin-coating methods. The deposited films with several hundred nanometers of thicknesses exhibited a strong preferred orientation along the *a*-axis direction. The chirality of the thin films was confirmed by solid-state CD spectroscopy revealing the opposite CPL absorption differences. The newly discovered chiral thin films are expected to be used as a useful platform for various surface interface reactions and applications. We are in the process of tuning the band gaps of the series OIHMs by controlling the halides and their stoichiometry for developing novel lead-free photovoltaic devices and will be reporting on them soon.

EXPERIMENTAL SECTION

Synthesis. (*R*)-(+)-1-Phenylethylamine ((*R*)-1-PEA, >99%), (*S*)-(−)-1-phenylethylamine ((*S*)-1-PEA, >99%), *N*,*N*′-dimethylformamide (DMF, anhydrous, 99.9%), bismuth(III) bromide ($BiBr_3$, 99.9%), and hydrobromic acid (HBr, 48 wt %) were purchased from Alfa Aesar. Single crystals of $[((R)\text{-}C_8H_{12}N)_4][Bi_2Br_{10}]$ [(*R*)-**1**] and $[((S)\text{-}C_8H_{12}N)_4][Bi_2Br_{10}]$ [(*S*)-**1**] were grown through a slow evaporation method. $BiBr_3$ (0.8×10^{-3} mol, 0.359 g) and (*R*)- or (*S*)-1-phenylethylamine (1.6×10^{-3} mol, 0.206 mL) were dissolved in 6 mL of a 48% HBr aqueous solution. After heating at 60 °C for 20 min, the solution mixtures were slowly cooled to room temperature. Yellow crystals of compounds (*R*)-**1** and (*S*)-**1** were grown in 2 days as the solvent was slowly evaporated.

Thin films of chiral compounds were prepared on square quartz plate substrates with a transmittance of 80% or more at low-wavelength (250 nm) regions. First, the substrate was ultrasonically treated with isopropyl alcohol for 10 min, and the substrate surface was further treated with oxygen plasma for 15 min. Crystals of compounds (*R*)-**1** and (*S*)-**1** were then dissolved in DMF to prepare the precursor solutions (20 wt %). Films were spin-coated on the clean substrates by taking

DOI: 10.1021/acsomega.8b02877
ACS Omega 2018, 3, 17895−17903

30 μL of the precursor solutions. The rate of the spin coater reached 2000 rpm in 2 s and the coating time was 30 s. The coated films were annealed at 80 °C for 10 min with a hot plate.

Structure Determination. Single-crystal X-ray diffraction (SCXRD) data for compound (*R*)-**1** were obtained using Bruker SMART BREEZE diffractometer on graphite-monochromated Mo Kα radiation (λ 0.71073 Å) and a 1 K charge coupled device (CCD) area detector at room temperature. The diffraction data for compound (*S*)-**1** were collected at room temperature on an ADSC Quantum-210 CCD diffractometer with synchrotron radiation (λ 0.63000 Å) at two-dimensional supramolecular crystallography at the Pohang Accelerator Laboratory, Korea. To monitor any possible phase transitions at lower temperatures, SCXRD data for each compound were also collected with the same synchrotron radiation method at 100 K. A yellow plate (0.200 mm × 0.139 mm × 0.122 mm) for compound (*R*)-**1** and a yellow plate (0.098 mm × 0.033 mm × 0.014 mm) for compound (*S*)-**1** were used for SCXRD measurements. The data were integrated using the SAINT (version 8.27A) program[56] or the HKL3000sm (version 703r) program.[57] Intensity correction was performed based on air absorption, polarization, and Lorentz factor. Semiempirical absorption correction was applied by the SADABS (version 2012/1) program[58] or HKL3000sm program. The crystal structures were solved and refined with the programs SHELXS-2013 and SHELXL-2013, respectively,[59] implemented in the WinGX-2014.[60] Relevant crystallographic information for compounds (*R*)-**1** and (*S*)-**1** is listed in Table 1.

Table 1. Crystallographic Data for (*R*)-1 and (*S*)-1

parameter	(*R*)-**1**	(*S*)-**1**
formula	$(C_8H_{12}N)_4Bi_2Br_{10}$	$(C_8H_{12}N)_4Bi_2Br_{10}$
FW (g mol^{-1})	1705.70	1705.70
space group	$P2_1$ (no. 4)	$P2_1$ (no. 4)
a (Å)	11.9962(3)	11.997(2)
b (Å)	14.6765(4)	14.728(3)
c (Å)	13.8899(4)	13.940(3)
β (Å)	93.394(2)	93.44(9)
V (Å^3)	2441.20(11)	2458.7(9)
Z	2	2
$D_{calc.}$ (g cm^{-3})	2.321	2.304
λ (Å)	0.71073	0.63
T (K)	296	296
R(int)	0.050	0.064
$R(F)^a$	0.032	0.037
$R_w(F_o^2)^b$	0.060	0.088
Flack *x*	−0.014(6)	0.000(5)

$^aR(F) = \sum||F_o| - |F_c||/\sum|F_o|$. $^bR_w(F_o^2) = \{\sum w[(F_o)^2 - (F_c)^2]^2/\sum w[(F_o)^2]^2\}^{1/2}$.

Powder X-ray diffraction (PXRD) data were obtained at room temperature using a Bruker D8 ADVANCE diffractometer with Cu Kα radiation (λ 1.5418 Å). Samples mounted on glass sample holders were scanned in the 2θ range of 5−70° with the step size and step time of 0.02° and 0.1 s, respectively. Phase purity of the samples was verified by comparing the calculated data obtained from single-crystal X-ray diffraction model with the measured PXRD patterns. The chirality of the two enantiomer compounds (*R*)-**1** and (*S*)-**1** could not be distinguished from the PXRD data.

Characterization. The dipole moment calculations for organic molecules were performed with the Gaussian 09 package.[61] The geometries of the organic molecules were determined via the SCXRD data and self-consistent field (SCF) energy calculation was performed without optimization. All the atoms were calculated at the density functional B3PW91/6-311G(d, p) level.[62]

The electronic band gap of the compound (*R*)-**1** was investigated using density function theory (DFT) calculation methods. The SCXRD data were used for structural optimization. All the calculations were implemented via open-source PWscf code in Quantum Espresso package.[63] Ultrasoft pseudopotentials[64] with nonlinear core correction[65] and the Perdew−Burke−Ernzerhof[66] exchange−correlation functional were used for all elements (Bi, Br, C, N, and H). The plane-wave kinetic energy and charge density cutoffs used in the SCF calculations were ca. 56 and 506 Ry, respectively, and a 3 × 3 × 3 grid was used for Brillouin zone sampling. The convergence threshold of the ground state energy was set to 1.0×10^{-6} Ry.

IR spectra of compounds (*R*)-**1** and (*S*)-**1** were collected using a Nicolet 6700 FT-IR spectrometer in the spectral range of 400−4000 cm^{-1} at room temperature with the prepared pellets. Approximately 1 mg of powder samples were intimately ground with 100 mg of predried KBr and compressed into transparent disk-shaped pellets.

UV−vis diffuse reflectance spectra for compounds (*R*)-**1** and (*S*)-**1** were measured on a Varian Cary 500 scan UV−vis NIR spectrometer at room temperature in the range of 200−2500 nm. The band gap energy was calculated using the following Kubelka−Munk function[67,68]

$$F(R) = \frac{(1-R)^2}{2R} = \frac{K}{S}$$

where *S*, *K*, and *R* represent the scattering coefficient, absorption coefficient, and reflectance, respectively. The plotted graphs of *F*(*R*) versus *hν* of compounds (*R*)-**1** and (*S*)-**1** resulted in the calculated band gap, E_g, of 2.88 eV.

Circular dichroism (CD) spectra (400−180 nm) for compounds (*R*)-**1** and (*S*)-**1** films spin-coated in quartz plates were measured on JASCO J-815 CD spectrometer. Chiral thin films of (*R*)-**1** and (*S*)-**1** were measured in a CD module with nitrogen gas purged, and the background was nondeposited quartz plate. Scanning speed and data interval were measured at 100 nm min^{-1} and 0.5 nm, respectively. The integrating sphere was used to collect the scattered light into the detector. The CD spectra of background and thin films were obtained by averaging 3 scans. The high-tension (HT) voltage of the photomultiplier tube detector was set not to exceed 800 V to collect reliable CD data. The anisotropy factor (*g*) was calculated according to the following formula

$$g = \frac{\Delta A}{A} = \frac{\text{CD (mdeg)}}{32\,980 \times A}$$

where Δ*A* and *A* represent the absorbance difference between the left and the right circularly polarized light of the sample and the absorbance of unpolarized light, respectively.[49]

Thermogravimetric analysis (TGA) was conducted on a SCINCO TGA N1000 thermal analyzer from room temperature to 900 °C with an increasing rate of 10 °C min^{-1} under flowing argon.

DOI: 10.1021/acsomega.8b02877
ACS Omega 2018, 3, 17895−17903

Scanning electron microscope (SEM)−energy-dispersive analysis by X-ray (EDX) analyses for compounds (*R*)-**1** and (*S*)-**1** were performed on Hitachi S-3400N and Horiba Energy EX-250 instruments. Elemental analysis was performed on a Carlo Erba EA 1108 CHNS_O analyzer at the Organic Chemistry Research Center, Sogang University. The atomic ratios obtained by EDX and EA agreed well with the chemical formulae obtained from the SCXRD data. The EDX data reveal that the atomic ratio of Bi and Br for both (*R*)-**1** and (*S*)-**1** was 1.0:5.0 (Figure S1a). Calculated element ratio: C, 22.53%; H, 2.84%; N, 3.28%, EA analysis data of (*R*)-**1**: C, 22.53%; H, 2.83%; N, 3.24%, and (*S*)-**1**: C, 22.54%; H, 2.86%; N, 3.26%.

The surface and cross-sectional information of the chiral thin film was obtained by FE-SEM by a Carl Zeiss SIGMA instrument with the InLens and type II secondary electrons (SE2) detectors.

To determine the SHG efficiency, crystals of compounds (*R*)-**1** and (*S*)-**1** were finely ground and sieved into different particle size ranges (<20, 20−45, 45−63, 63−90, 90−125, and 125−150 μm). The sieved powder samples were loaded into different capillary tubes and the SHG was measured using a DAWA Q-switched Nd:YAG laser (1064 nm radiation at 20 Hz). The SHG of polycrystalline α-SiO_2 with the same particle size ranges was also measured as standard materials and the efficiencies were compared.

■ ASSOCIATED CONTENT

Supporting Information

The Supporting Information is available free of charge on the ACS Publications website at DOI: 10.1021/acsomega.8b02877.

Selected bond distances and angles, bond valence sum calculations, octahedral distortion calculations, hydrogen bond geometry, dipole moment calculations, EDX, ORTEP drawings, TGA, and IR spectrum (PDF)

Crystallographic data of CCDC 1873000−1873001 (CIF)

■ AUTHOR INFORMATION

Corresponding Author

*E-mail: kmok@cau.ac.kr. Tel: +82-2-820-5197.

ORCID

Tae Hwan Moon: 0000-0003-2884-323X

Kang Min Ok: 0000-0002-7195-9089

Notes

The authors declare no competing financial interest.

■ ACKNOWLEDGMENTS

This research was supported by the Chung-Ang University Graduate Research Scholarship in 2018. This research was also supported by the National Research Foundation of Korea (NRF) funded by the Ministry of Science and ICT (Grant Nos 2016R1A2A2A05005298 and 2018R1A5A1025208).

■ REFERENCES

(1) Sun, Z.; Liu, X.; Khan, T.; Ji, C.; Asghar, M. A.; Zhao, S.; Li, L.; Hong, M.; Luo, J. A Photoferroelectric Perovskite-Type Organometallic Halide with Exceptional Anisotropy of Bulk Photovoltaic Effects. *Angew. Chem., Int. Ed.* **2016**, *55*, 6545−6550.

(2) Sun, Z.; Zeb, A.; Liu, S.; Ji, C.; Khan, T.; Li, L.; Hong, M.; Luo, J. Exploring a Lead-free Semiconducting Hybrid Ferroelectric with a Zero-Dimensional Perovskite-like Structure. *Angew. Chem., Int. Ed.* **2016**, *55*, 11854−11858.

(3) Cho, H.; Kim, Y. H.; Wolf, C.; Lee, H. D.; Lee, T. W. Improving the Stability of Metal Halide Perovskite Materials and Light-Emitting Diodes. *Adv. Mater.* **2018**, *30*, No. 1704587.

(4) Kim, Y. H.; Cho, H.; Lee, T. W. Metal halide perovskite light emitters. *Proc. Natl. Acad. Sci. U.S.A.* **2016**, *113*, 11694−11702.

(5) Deng, W.; Xu, X.; Zhang, X.; Zhang, Y.; Jin, X.; Wang, L.; Lee, S. T.; Jie, J. Organometal Halide Perovskite Quantum Dot Light-Emitting Diodes. *Adv. Funct. Mater.* **2016**, *26*, 4797−4802.

(6) Wang, H.; Kim, D. H. Perovskite-based photodetectors: materials and devices. *Chem. Soc. Rev.* **2017**, *46*, 5204−5236.

(7) Chen, S.; Shi, G. Two-Dimensional Materials for Halide Perovskite-Based Optoelectronic Devices. *Adv. Mater.* **2017**, *29*, No. 1605448.

(8) Ahmadi, M.; Wu, T.; Hu, B. A Review on Organic-Inorganic Halide Perovskite Photodetectors: Device Engineering and Fundamental Physics. *Adv. Mater.* **2017**, *29*, No. 1605242.

(9) Zhao, H.; Li, Y.; Zhang, B.; Xu, T.; Wang, C. PtI_x/$[(CH_3)_2NH_2]_3[BiI_6]$ as a well-dispersed photocatalyst for hydrogen production in hydroiodic acid. *Nano Energy* **2018**, *50*, 665−674.

(10) Hwang, J.; Rao, R. R.; Giordano, L.; Katayama, Y.; Yu, Y.; Shao-Horn, Y. Perovskites in catalysis and electrocatalysis. *Science* **2017**, *358*, 751−756.

(11) Park, S.; Chang, W. J.; Lee, C. W.; Park, S.; Ahn, H.-Y.; Nam, K. T. Photocatalytic hydrogen generation from hydriodic acid using methylammonium lead iodide in dynamic equilibrium with aqueous solution. *Nat. Energy* **2016**, *2*, No. 16185.

(12) Chen, Y. T.; Wu, X. H.; Chu, Y. L.; Zhou, J. C.; Zhou, B. L.; Huang, J. Hybrid Field-Effect Transistors and Photodetectors Based on Organic Semiconductor and $CsPbI_3$ Perovskite Nanorods Bilayer Structure. *Nano-Micro Lett.* **2018**, *10*, 57.

(13) Zhu, H.; Fu, Y.; Meng, F.; Wu, X.; Gong, Z.; Ding, Q.; Gustafsson, M. V.; Trinh, M. T.; Jin, S.; Zhu, X. Y. Lead halide perovskite nanowire lasers with low lasing thresholds and high quality factors. *Nat. Mater.* **2015**, *14*, 636−642.

(14) Fu, Y.; Zhu, H.; Schrader, A. W.; Liang, D.; Ding, Q.; Joshi, P.; Hwang, L.; Zhu, X. Y.; Jin, S. Nanowire Lasers of Formamidinium Lead Halide Perovskites and Their Stabilized Alloys with Improved Stability. *Nano Lett.* **2016**, *16*, 1000−1008.

(15) Yuan, C.; Li, X.; Semin, S.; Feng, Y.; Rasing, T.; Xu, J. Chiral Lead Halide Perovskite Nanowires for Second-Order Nonlinear Optics. *Nano Lett.* **2018**, *18*, 5411−5417.

(16) Kubicki, D. J.; Prochowicz, D.; Hofstetter, A.; Saski, M.; Yadav, P.; Bi, D.; Pellet, N.; Lewinski, J.; Zakeeruddin, S. M.; Gratzel, M.; Emsley, L. Formation of Stable Mixed Guanidinium-Methylammonium Phases with Exceptionally Long Carrier Lifetimes for High-Efficiency Lead Iodide-Based Perovskite Photovoltaics. *J. Am. Chem. Soc.* **2018**, *140*, 3345−3351.

(17) Liao, Y.; Liu, H.; Zhou, W.; Yang, D.; Shang, Y.; Shi, Z.; Li, B.; Jiang, X.; Zhang, L.; Quan, L. N.; Quintero-Bermudez, R.; Sutherland, B. R.; Mi, Q.; Sargent, E. H.; Ning, Z. Highly Oriented Low-Dimensional Tin Halide Perovskites with Enhanced Stability and Photovoltaic Performance. *J. Am. Chem. Soc.* **2017**, *139*, 6693−6699.

(18) Li, T.; Hu, Y.; Morrison, C. A.; Wu, W.; Han, H.; Robertson, N. Lead-free pseudo-three-dimensional organic−inorganic iodobismuthates for photovoltaic applications. *Sustainable Energy Fuels* **2017**, *1*, 308−316.

(19) Hoefler, S. F.; Trimmel, G.; Rath, T. Progress on lead-free metal halide perovskites for photovoltaic applications: a review. *Monatsh. Chem.* **2017**, *148*, 795−826.

(20) Shi, D.; Adinolfi, V.; Comin, R.; Yuan, M.; Alarousu, E.; Buin, A.; Chen, Y.; Hoogland, S.; Rothenberger, A.; Katsiev, K.; Losovyj, Y.; Zhang, X.; Dowben, P. A.; Mohammed, O. F.; Sargent, E. H.; Bakr, O. M. Solar cells. Low trap-state density and long carrier diffusion in organolead trihalide perovskite single crystals. *Science* **2015**, *347*, 519−522.

(21) Xing, G.; Mathews, N.; Lim, S. S.; Yantara, N.; Liu, X.; Sabba, D.; Gratzel, M.; Mhaisalkar, S.; Sum, T. C. Low-temperature solution-

DOI: 10.1021/acsomega.8b02877
ACS Omega 2018, 3, 17895−17903

processed wavelength-tunable perovskites for lasing. *Nat. Mater.* **2014**, *13*, 476−480.
(22) Stranks, S. D.; Eperon, G. E.; Grancini, G.; Menelaou, C.; Alcocer, M. J.; Leijtens, T.; Herz, L. M.; Petrozza, A.; Snaith, H. J. Electron-hole diffusion lengths exceeding 1 micrometer in an organometal trihalide perovskite absorber. *Science* **2013**, *342*, 341−344.
(23) Kazmerski, L. *Best Research-Cell Efficiencies Chart*; National Renewable Energy Laboratory, 2012. https://www.nrel.gov/ncpv/images/efficiency_chart.jpg.
(24) Ahn, J.; Lee, E.; Tan, J.; Yang, W.; Kim, B.; Moon, J. A new class of chiral semiconductors: chiral-organic-molecule-incorporating organic−inorganic hybrid perovskites. *Mater. Horiz.* **2017**, *4*, 851−856.
(25) Peng, Y.; Yao, Y.; Li, L.; Wu, Z.; Wang, S.; Luo, J. White-light emission in a chiral one-dimensional organic−inorganic hybrid perovskite. *J. Mater. Chem. C* **2018**, *6*, 6033−6037.
(26) Slikkerveer, A.; de Wolff, F. A. Pharmacokinetics and toxicity of bismuth compounds. *Med. Toxicol. Adverse Drug Exper.* **1989**, *4*, 303−323.
(27) Liang, L.; Gao, P. Lead-Free Hybrid Perovskite Absorbers for Viable Application: Can We Eat the Cake and Have It too? *Adv. Sci.* **2018**, *5*, No. 1700331.
(28) Zhang, W.; Tao, K.; Ji, C.; Sun, Z.; Han, S.; Zhang, J.; Wu, Z.; Luo, J. $(C_6H_{13}N)_2BiI_5$: A One-Dimensional Lead-Free Perovskite-Derivative Photoconductive Light Absorber. *Inorg. Chem.* **2018**, *57*, 4239−4243.
(29) Zhang, W. C.; Liu, X. T.; Li, L. N.; Sun, Z. H.; Han, S. G.; Wu, Z. Y.; Luo, J. H. Triiodide-Induced Band-Edge Reconstruction of a Lead-Free Perovskite-Derivative Hybrid for Strong Light Absorption. *Chem. Mater.* **2018**, *30*, 4081−4088.
(30) García-Fernández, A.; Marcos-Cives, I.; Platas-Iglesias, C.; Castro-Garcia, S.; Vazquez-Garcia, D.; Fernandez, A.; Sanchez-Andujar, M. Diimidazolium Halobismuthates $[Dim]_2[Bi_2X_{10}]$ (X Cl^-, Br^-, or I^-): A New Class of Thermochromic and Photoluminescent Materials. *Inorg. Chem.* **2018**, *57*, 7655−7664.
(31) Adonin, S. A.; Sokolov, M. N.; Fedin, V. P. Bismuth(III) Halide Complexes: New Structural Types and New Application Areas. *Russ. J. Inorg. Chem.* **2017**, *62*, 1789−1796.
(32) Zheng, X. X.; Liu, Y.; Liu, G. F.; Liu, J.; Ye, X.; Han, Q. X.; Ge, C.; Tao, X. T. Crystalline Mixed Halide Halobismuthates and Their Induced Second Harmonic Generation. *Chem. Mater.* **2016**, *28*, 4421−4431.
(33) Węcławik, M.; Gągor, A.; Jakubas, R.; Piecha-Bisiorek, A.; Medycki, W.; Baran, J.; Zieliński, P.; Gałązka, M. Structure−property relationships in hybrid $(C_3H_5N_2)_3[Sb_2I_9]$ and $(C_3H_5N_2)_3[Bi_2I_9]$ isomorphs. *Inorg. Chem. Front.* **2016**, *3*, 1306−1316.
(34) Dammak, H.; Yangui, A.; Triki, S.; Abid, Y.; Feki, H. Structural characterization, vibrational, optical properties and DFT investigation of a new luminescent organic−inorganic material: $(C_6H_{14}N)_3Bi_2I_9$. *J. Lumin.* **2015**, *161*, 214−220.
(35) Attia, S.; Chaari, N.; Chaabouni, S. Synthesis, crystal structure, and dielectric properties of (3-aminopropyl-imidazolium) pentachlorobismuthate (III) $[C_6H_{13}N_3]BiCl_5$. *J. Cluster Sci.* **2015**, *26*, 1343−1359.
(36) Leblanc, N.; Mercier, N.; Zorina, L.; Simonov, S.; Auban-Senzier, P.; Pasquier, C. Large spontaneous polarization and clear hysteresis loop of a room-temperature hybrid ferroelectric based on mixed-halide $[BiI_3Cl_2]$ polar chains and methylviologen dication. *J. Am. Chem. Soc.* **2011**, *133*, 14924−14927.
(37) Nandhini, S.; Sudhakar, K.; Muniyappan, S.; Murugakoothan, P. Systematic discussions on structural, optical, mechanical, electrical and its application to NLO devices of a novel semi-organic single crystal: Guanidinium tetrafluoroborate (GFB). *Opt. Laser Technol.* **2018**, *105*, 249−256.
(38) Ok, K. M.; Chi, E. O.; Halasyamani, P. S. Bulk characterization methods for non-centrosymmetric materials: second-harmonic generation, piezoelectricity, pyroelectricity, and ferroelectricity. *Chem. Soc. Rev.* **2006**, *35*, 710−717.
(39) Laane, J.; Jagodzinski, P. W. Low-Frequency Vibrational-Spectra of Bromo-Bismuthates and Iodo-Bismuthates and the Observation of a Trans Effect. *Inorg. Chem.* **1980**, *19*, 44−49.
(40) Brese, N.; O'keeffe, M. Bond-valence parameters for solids. *Acta Crystallogr., Sect. B: Struct. Sci.* **1991**, *47*, 192−197.
(41) Liao, W.-Q.; Zhang, Y.; Hu, C.-L.; Mao, J.-G.; Ye, H.-Y.; Li, P.-F.; Huang, S. D.; Xiong, R.-G. A lead-halide perovskite molecular ferroelectric semiconductor. *Nat. Commun.* **2015**, *6*, No. 7338.
(42) García-Fernández, A.; Bermudez-Garcia, J. M.; Castro-Garcia, S.; Llamas-Saiz, A. L.; Artiaga, R.; Lopez-Beceiro, J. J.; Sanchez-Andujar, M.; Senaris-Rodriguez, M. A. $[(CH_3)_2NH_2]_7Pb_4X_{15}$ (X Cl^- and Br^-), 2D-Perovskite Related Hybrids with Dielectric Transitions and Broadband Photoluminiscent Emission. *Inorg. Chem.* **2018**, *57*, 3215−3222.
(43) Leng, M.; Chen, Z.; Yang, Y.; Li, Z.; Zeng, K.; Li, K.; Niu, G.; He, Y.; Zhou, Q.; Tang, J. Lead-Free, Blue Emitting Bismuth Halide Perovskite Quantum Dots. *Angew. Chem., Int. Ed.* **2016**, *55*, 15012−15016.
(44) Li, M.-Q.; Hu, Y.-Q.; Bi, L.-Y.; Zhang, H.-L.; Wang, Y.; Zheng, Y.-Z. Structure Tunable Organic−Inorganic Bismuth Halides for an Enhanced Two-Dimensional Lead-Free Light-Harvesting Material. *Chem. Mater.* **2017**, *29*, 5463−5467.
(45) Berova, N.; Di Bari, L.; Pescitelli, G. Application of electronic circular dichroism in configurational and conformational analysis of organic compounds. *Chem. Soc. Rev.* **2007**, *36*, 914−931.
(46) Ben-Moshe, A.; Teitelboim, A.; Oron, D.; Markovich, G. Probing the Interaction of Quantum Dots with Chiral Capping Molecules Using Circular Dichroism Spectroscopy. *Nano Lett.* **2016**, *16*, 7467−7473.
(47) Macleod, N. A.; Butz, P.; Simons, J. P.; Grant, G. H.; Baker, C. M.; Tranter, G. E. Structure, electronic circular dichroism and Raman optical activity in the gas phase and in solution: a computational and experimental investigation. *Phys. Chem. Chem. Phys.* **2005**, *7*, 1432−1440.
(48) Smith, H. E.; Neergaard, J. R.; Depaulis, T.; Chen, F. M. Optically-Active Amines. 31. Spectral Observations on the Substituted Benzene Chromophore. *J. Am. Chem. Soc.* **1983**, *105*, 1578−1584.
(49) He, T. C.; Li, J. Z.; Li, X. R.; Ren, C.; Luo, Y.; Zhao, F. H.; Chen, R.; Lin, X. D.; Zhang, J. M. Spectroscopic studies of chiral perovskite nanocrystals. *Appl. Phys. Lett.* **2017**, *111*, No. 151102.
(50) Knoppe, S.; Dolamic, I.; Dass, A.; Burgi, T. Separation of enantiomers and CD spectra of $Au_{40}(SCH_2CH_2Ph)_{24}$: spectroscopic evidence for intrinsic chirality. *Angew. Chem., Int. Ed.* **2012**, *51*, 7589−7591.
(51) Xiao, Z.; Meng, W.; Wang, J.; Yan, Y. Thermodynamic Stability and Defect Chemistry of Bismuth-Based Lead-Free Double Perovskites. *ChemSusChem* **2016**, *9*, 2628−2633.
(52) Kurtz, S. K.; Perry, T. T. A Powder Technique for the Evaluation of Nonlinear Optical Materials. *J. Appl. Phys.* **1968**, *39*, 3798−3813.
(53) Nguyen, S. D.; Yeon, J.; Kim, S. H.; Halasyamani, P. S. $BiO(IO_3)$: a new polar iodate that exhibits an aurivillius-type $(Bi_2O_2)^{2+}$ layer and a large SHG response. *J. Am. Chem. Soc.* **2011**, *133*, 12422−12425.
(54) Sun, C. F.; Hu, C. L.; Xu, X.; Ling, J. B.; Hu, T.; Kong, F.; Long, X. F.; Mao, J. G. $BaNbO(IO_3)_5$: a new polar material with a very large SHG response. *J. Am. Chem. Soc.* **2009**, *131*, 9486−9487.
(55) Sykora, R. E.; Ok, K. M.; Halasyamani, P. S.; Albrecht-Schmitt, T. E. Structural modulation of molybdenyl iodate architectures by alkali metal cations in $AMoO_3(IO_3)$(A K, Rb, Cs): a facile route to new polar materials with large SHG responses. *J. Am. Chem. Soc.* **2002**, *124*, 1951−1957.
(56) *SAINT: Area-Detector Integration Software, Siemens Analytical X-ray Instruments*; Bruker: Madison, WI, 2013.
(57) Minor, W.; Cymborowski, M.; Otwinowski, Z.; Chruszcz, M. HKL-3000: the integration of data reduction and structure solution - from diffraction images to an initial model in minutes. *Acta Crystallogr., Sect. D: Biol. Crystallogr.* **2006**, *62*, 859−866.

DOI: 10.1021/acsomega.8b02877
ACS Omega 2018, 3, 17895−17903

(58) Sheldrick, G. M. *SHELX-2013—Programs for Crystal Structure Analysis: i. Structure Determination (SHELXS) and ii. Refinement (SHELXL-2013)*; University of Gottingen: Germany, 2013.
(59) Sheldrick, G. M. *SADABS*; University of Göttingen: Germany, 2013.
(60) Farrugia, L. J. WinGX and ORTEP for Windows: an update. *J. Appl. Crystallogr.* **2012**, *45*, 849−854.
(61) Frisch, M.; Trucks, G.; Schlegel, H.; Scuseria, G.; Robb, M.; Cheeseman, J.; Scalmani, G.; Barone, V.; Mennucci, B.; Petersson, G. *Gaussian 09*; Gaussian Inc.: Pittsburgh, PA, 2009.
(62) Scott, A. P.; Radom, L. Harmonic vibrational frequencies: an evaluation of Hartree− Fock, Møller− Plesset, quadratic configuration interaction, density functional theory, and semiempirical scale factors. *J. Phys. Chem.* **1996**, *100*, 16502−16513.
(63) Giannozzi, P.; Baroni, S.; Bonini, N.; Calandra, M.; Car, R.; Cavazzoni, C.; Ceresoli, D.; Chiarotti, G. L.; Cococcioni, M.; Dabo, I.; et al. QUANTUM ESPRESSO: a modular and open-source software project for quantum simulations of materials. *J. Phys.: Condens. Matter* **2009**, *21*, No. 395502.
(64) Vanderbilt, D. Soft self-consistent pseudopotentials in a generalized eigenvalue formalism. *Phys. Rev. B* **1990**, *41*, 7892−7895.
(65) Louie, S. G.; Froyen, S.; Cohen, M. L. Nonlinear ionic pseudopotentials in spin-density-functional calculations. *Phys. Rev. B* **1982**, *26*, 1738.
(66) Perdew, J. P.; Burke, K.; Ernzerhof, M. Generalized Gradient Approximation Made Simple. *Phys. Rev. Lett.* **1996**, *77*, 3865−3868.
(67) Kubelka, P. Ein Beitrag zur Optik der Farbanstriche (Contribution to the optic of paint). *Z. Tech. Phys.* **1931**, *12*, 593−601.
(68) Tauc, J. Absorption edge and internal electric fields in amorphous semiconductors. *Mater. Res. Bull.* **1970**, *5*, 721−729.

DOI: 10.1021/acsomega.8b02877
ACS Omega 2018, 3, 17895−17903